Progress in Natural Science: Materials International 36 (2026) 84–93

Contents lists available at ScienceDirect

Progress in Natural Science: Materials International

journal homepage: www.elsevier.com/locate/pnsmi

Enhancing photocatalytic nitrogen fixation through controlled acid corrosion of 1D TiO_2 nanobelts

Guanzheng Liu[a], Mengyu Wang[a], Jianing Huang[a], Chunyuan Li[a], Junkai Ren[b,*], Qi Wang[a], Haili Pang[a], Hui Zhang[a], Xiaoxia Bai[a,**]

[a] *Key Laboratory of High-Orbits-Electron Materials and Protection Technology for Aerospaceare, School of Advanced Materials and Nanotechnology, Xidian University, Xi'an, 710126, China*
[b] *School of Physics, Xidian University, Xi'an, 710126, China*

ARTICLE INFO

Keywords:
TiO_2 nanobelt
Hydrothermal synthesis
Acid corrosion
Photocatalytic nitrogen reduction
Ammonia

ABSTRACT

Photocatalytic nitrogen reduction to produce ammonia under ambient conditions is a promising green route. In this study, we demonstrate that one-dimensional (1D) TiO_2 nanobelts, prepared via a facile hydrothermal method, can convert gaseous dinitrogen to ammonia in pure water under light irradiation. The photocatalytic ammonia production performance of TiO_2 nanobelts can be further enhanced through acid corrosion treatment, which generates secondary nanostructures. These surface nanostructures serve as potential catalytically active sites for nitrogen adsorption and reduction. Both photoelectrochemical measurements and photoluminescence spectra confirm that the optimized TiO_2 nanobelts exhibit improved charge separation. Given their excellent stability and unique 1D nanostructure, acid-corroded TiO_2 nanobelts are a promising support material for constructing high-performance composite photocatalysts for nitrogen fixation.

1. Introduction

Ammonia, one of the most essential industrial chemicals, is primarily produced through two pathways: the natural biogeochemical nitrogen cycle and the energy-intensive Haber-Bosch process [1]. While the former cannot meet the growing demand driven by population growth and economic development, the latter raises significant environmental and energy sustainability concerns [2,3]. Photocatalytic nitrogen fixation, which utilizes solar energy to convert atmospheric nitrogen to ammonia under ambient conditions, has emerged as a promising green alternative [4]. This process shares fundamental mechanisms with photocatalytic water splitting [5,6], involving: (1) light absorption by photosensitizers, (2) generation of electron-hole pairs, (3) charge separation and transport, and (4) interfacial redox reactions [7,8]. However, nitrogen fixation presents greater challenges due to the high energy barrier of $N\equiv N$ bond dissociation (941 kJ mol^{-1}) and the low solubility of N_2 in aqueous systems [6,9].

Recent years have witnessed remarkable progress in both photocatalyst development and mechanistic understanding [10–13]. Nevertheless, the search for more efficient photocatalysts remains an active research frontier [6,14–16]. The reduction process relies on photogenerated electrons from the photocatalyst's conduction band, where reducing power is determined by the energy difference between the conduction band minimum (CBM) and the N_2/NH_3 redox potential (-0.092 V vs. SHE at pH 7). Thermodynamically, the CBM must be more negative than the N_2/NH_3 potential, while the valence band maximum (VBM) should be more positive than the H_2O/O_2 potential (1.23 V vs. SHE) [6]. Although higher CBM positions enhance reducing capability, they typically require wider bandgap semiconductors (e.g.,TiO_2 [17,18], diamond [19] and GaN nanowires [20]), that only absorb UV light (<5 % of solar spectrum) [5]. Beyond their limited light absorption range, the primary challenges faced by these wide-bandgap semiconductors in photocatalytic nitrogen fixation also encompass low charge separation efficiency, high energy barriers for nitrogen activation, and competing side reactions [21]. Current research strategies primarily address these issues through elemental doping, construction of heterojunctions, and the introduction of defects [22]. However, relatively little attention has been devoted to enhancing the UV activity and improving charge separation efficiency in wide-bandgap semiconductor catalysts via structural modulation [23].

---

* Corresponding author.
** Corresponding author.
E-mail addresses: renjunkai@xidian.edu.cn (J. Ren), xxbai@xidian.edu.cn (X. Bai).

https://doi.org/10.1016/j.pnsc.2025.11.004
Received 5 August 2025; Received in revised form 30 October 2025; Accepted 4 November 2025

Nanostructured TiO_2 has been extensively studied for environmental and energy applications [24–27]. The pioneering report of photocatalytic ammonia synthesis used Fe-doped TiO_2 [28]. In comparison with particulate TiO_2, one-dimensional TiO_2 nanobelts demonstrate distinct advantages in photocatalytic nitrogen fixation, primarily due to their ability to synergistically address two fundamental challenges, including efficient charge separation and effective nitrogen activation. The high aspect ratio and well-ordered structure of these nanobelts provide a direct and rapid transport pathway for photogenerated electrons, thereby significantly suppressing electron-hole recombination and enabling more electrons to participate in the nitrogen reduction process. Furthermore, the one-dimensional architecture offers a large specific surface area along with abundant edge and defect sites, which facilitate the adsorption and activation of the highly stable N_2 molecules [29]. Notably, Zhang et al. successfully achieved the conversion of N_2 to NH_3 under visible and near-infrared light without sacrificial agents by employing defective TiO_2 nanobamboo arrays, achieving a high selectivity NH_3 production rate of 48.3 mg m^{-2} h^{-1} [30].

This study introduces a hydrothermal acid-etching method to engineer surface nanostructures on TiO_2 nanobelts, significantly enhancing their photocatalytic nitrogen reduction activity. Mechanistic investigations reveal that the created surface structures promote interfacial charge transfer and accelerate surface reaction kinetics. Our findings provide a viable strategy for developing high-performance ammonia synthesis catalysts.

2. Experimental

2.1. Photocatalysts preparation

TiO_2 nanobelts were synthesized via a hydrothermal method following previously reported procedures [31,32], as outlined in Scheme 1a. Briefly, 0.3 g of P25 TiO_2 was homogeneously mixed with 60 mL of 10 M NaOH solution, transferred into a 100 mL Teflon-lined stainless-steel autoclave, and heated at 180 °C for 48 h. The resulting product was collected by filtration and subjected to ion exchange by dispersion in 500 mL of 0.1 M HCl aqueous solution for 48 h (repeated twice). After thorough washing with deionized water, the material was dried at 70 °C for 12 h. For hydrothermal acid corrosion, 0.3 g of the as-synthesized sample was treated with 20 mL of 0.02 M H_2SO_4 aqueous solution at 100 °C for varying durations (6–24 h). The acid-treated products were washed, dried (70 °C, 12 h), and annealed in air at

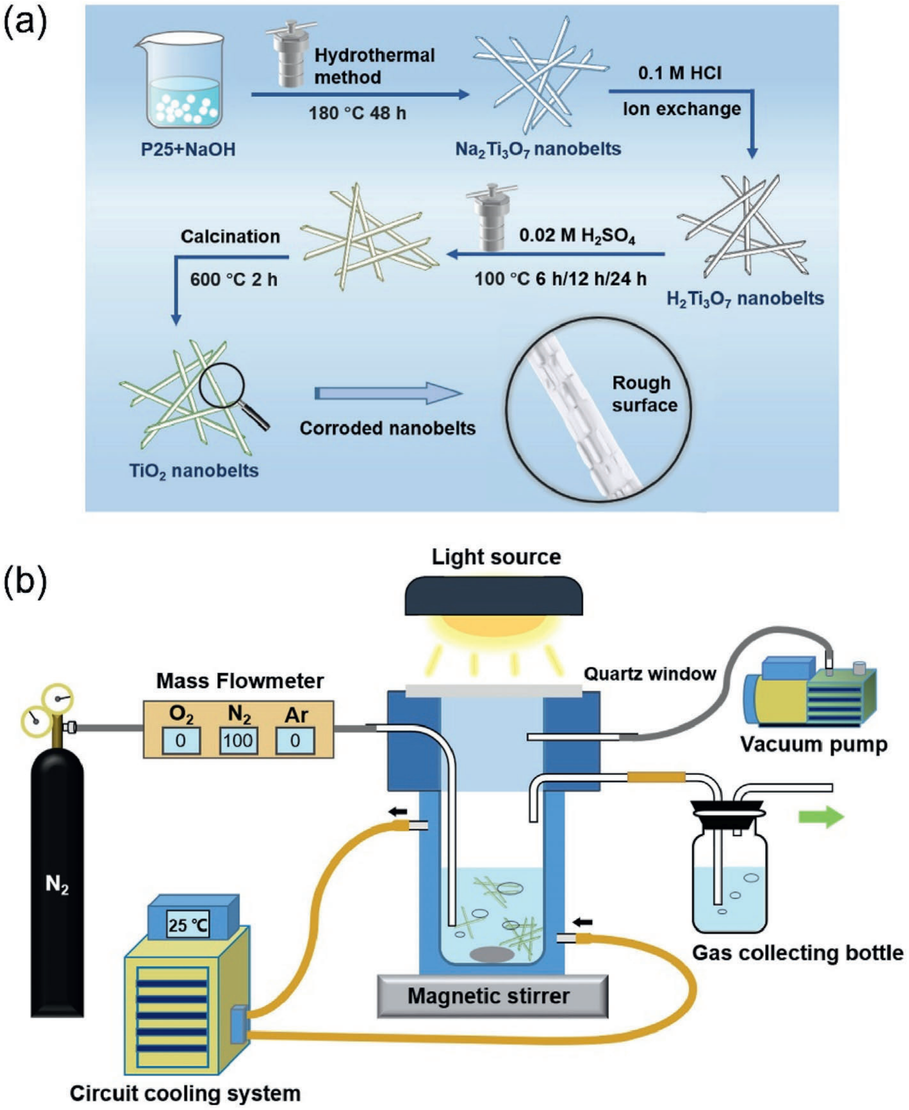

Scheme. 1. The schematic illustration of (a) the synthetic process of acid-corroded 1D TiO_2 nanobelts and (b) experimental setup for the investigation of the photocatalytic nitrogen fixation.

600 °C for 2 h to remove residual organic impurities. The final samples were labeled as TiO_2-6 h, TiO_2-12 h, and TiO_2-24 h based on corrosion time.

2.2. Characterization

The morphological features of the synthesized TiO_2 were characterized using scanning electron microscopy (SEM, FEI Apreo + HiVac) and transmission electron microscopy (TEM, JEOL 2100F). The specific surface area was determined by nitrogen adsorption-desorption measurements using an Automated Surface Area & Pore Size Analyzer (Quantachrome Autosorb iQ). Crystal structure analysis was performed via powder X-ray diffraction (XRD, Bruker D8 Advance) with Cu Kα radiation ($\lambda = 1.5406$ Å). Raman spectroscopy measurements were conducted on a Renishaw inVia spectrometer with 532 nm laser excitation. The origin of ammonia was verified by ^{15}N isotope labeling experiments using nuclear magnetic resonance spectroscopy (NMR, Bruker Avance 800). Surface defect characterization was carried out by electron spin resonance spectroscopy (ESR, Bruker EMXplus-6/1) at 77 K. UV–vis diffuse reflectance spectra were recorded on a Hitachi UH4150 spectrophotometer using $BaSO_4$ as a reflectance standard. Photoluminescence spectra were acquired at room temperature using a Renishaw inVia spectrometer with 325 nm laser excitation.

2.3. Photocatalytic N_2 fixation study

The photocatalytic performance of the synthesized TiO_2 was evaluated in a stainless-steel autoclave equipped with a thick quartz window, using a 300 W Xe lamp as the light source (Scheme 1b). Specifically, 30 mg of the TiO_2 photocatalyst was ultrasonically dispersed in 30 mL of ultrapure water, followed by magnetic stirring for 15 min to ensure homogeneity. The suspension was transferred into the autoclave, and the system was purged with ultrapure N_2 (flow rate: 100 mL min^{-1}) via multiple vacuum-refill cycles prior to illumination. During the photoreaction, a continuous N_2 flow was maintained, and the setup was temperature-controlled at 15 °C using a circulating water system. After 1 h of irradiation, the concentration of photogenerated ammonia was quantified by the indophenol blue method.

2.4. Detection of ammonia

The calibration curve for the indophenol-blue method was made firstly before the measurement of the photocatalytic produced ammonia. The standard NH_4Cl solution with the concentration of 0, 1, 2, 4, 6, 8, 16, 24 μmol L^{-1} was prepared, respectively (Fig. S1). Then the standard solutions (4 mL), salicylic acid (0.4 mL, 1.0 M in 1.17 M NaOH solution), sodium nitroprusside (0.025 mL, 1 wt%) and NaClO (0.025 mL, available chlorine content 0.35 wt% in 0.7 M NaOH), were sequentially added into the brown bottles, which were allowed to react in the dark for 1.5 h to achieve complete color development. Similarly, the photocatalytic produced ammonia was determined via this process that taking the photocatalytic reaction dispersion (3 mL) from the autoclave reactor and removing the catalyst by centrifugation. Afterwards, the obtained solutions reacted with the above solution of salicylic acid, sodium nitroprusside and NaClO, for 1.5 h in the dark at the room temperature. Then the amount of the produced ammonia was detected by evaluating the absorbance at 679 nm of the solution using the UV–vis spectrophotometer. 50 mg catalyst dispersed in 50 mL of ultrapure water, replaced the gas in the cavity with Ar for three times, introduced $^{15}N_2/^{14}N_2$ to atmospheric pressure, after 5 h of light, the pH value of the solution was adjusted to 2 with 2.5 M sulfuric acid, 0.4 mL of acidified solution was added to 0.1 mL of DMSO-d6 solution, and the mixed solution was tested by ^1H NMR. Take 30 μL of sample, add 30 μL of DMPO, mix well, and put it into the EPR sample cavity for superoxide and hydroxyl radical testing.

2.5. Photoelectrochemical measurements

Photoelectrochemical measurements were performed using a three-electrode configuration with a Solartron XM electrochemical workstation in 1 M NaOH electrolyte. A Pt plate and Hg/HgO electrode served as the counter and reference electrodes, respectively. The working electrode was fabricated using electrophoretic deposition in a two-electrode system. Specifically, 25 mg of catalyst were dispersed in 25 mL of acetone via sonication for 2 h, followed by the addition of 6 mg iodine under continuous magnetic stirring to ensure complete dissolution. Two FTO substrates (1.2 × 2 cm) were immersed in the resulting suspension, and a 10 V DC potential was applied for 5 min to deposit the catalyst. The coated FTO electrodes were vacuum-dried at 80 °C for 3 h to remove residual solvents. Electrical contacts were established by attaching copper wires to the FTO using silver paste, and insulated with AB epoxy. Mott-Schottky analysis was conducted in the dark over a potential range of −1 to 0 V (vs. Hg/HgO) using a 10 mV AC amplitude at 1320 Hz. The photocurrent response was evaluated at open-circuit potential under steady illumination.

3. Results and discussion

The morphology of the prepared samples was characterized by SEM (Fig. 1a–d). Pristine TiO_2 nanobelts (without acid corrosion) exhibit smooth surfaces and typical lengths of several microns. As the acid corrosion duration increases, the nanobelt surfaces become progressively rougher. After 24 h of treatment, the belt-like structure fragments into particulate morphology. Statistical analyses of nanobelt widths and particle sizes are provided in Fig. S2.

TEM analysis further reveals structural details (Fig. 1e–h). Fig. 1e confirms the nanobelt morphology, while Fig. 1f shows HRTEM lattice fringes with a spacing of around 0.34 nm, corresponding to the (101) plane of TiO_2 with a [101] growth direction. The TiO_2-12 h sample retains its nanobelt morphology but displays significantly roughened surfaces (Fig. 1g). Acid-corroded nanobelts maintain the same 0.34 nm lattice spacing as pristine samples (Fig. 1h), but exhibit distinct grain boundaries. TEM imaging of acid-etched nanobelts further confirms surface defects, revealing a substantial increase in grain boundaries between newly formed nanoparticles and between nanoparticles and residual nanobelts (Fig. S3).

The crystalline phase and structure were characterized by XRD and Raman spectroscopy (Fig. 2a and b). As shown in Fig. 2a, pristine TiO_2 nanobelts and TiO_2-6 h exhibit mixed phases of anatase (JCPDS: 78–2486) and TiO_2(B) (JCPDS: 46–1237) [31]. In contrast, TiO_2-12 h and TiO_2-24 h display pure anatase phase. Raman spectroscopy corroborates these findings that the disappearance of TiO_2(B) vibration modes (Fig. 2b) confirms the mixed-phase nature of pristine TiO_2 and TiO_2-6 h, while TiO_2-12 h and TiO_2-24 h show exclusively anatase signatures [33,34]. Crystallite sizes of nanoparticles were calculated using the Scherrer equation based on XRD data (Table S1).

Fig. 2c shows the UV–vis DRS spectra. All the TiO_2 samples show sharp absorption edges at about 380 nm. Indicating that the acid corrosion treatment has no effect on the optical properties. Fig. 2d is the corresponding Tauc plots, from which we can see that the samples have the same bandgap of 3.2 eV, only response to UV light irradiation [35].

Characterizing the specific surface area is crucial for understanding the potential performance of TiO_2 in applications on photocatalysis, as it directly influences reactant adsorption capacity and active site density. To quantitatively assess this key parameter, we performed nitrogen adsorption/desorption isotherm measurements at 77 K on both the pristine and acid-corroded TiO_2 samples, using the well-established Brunauer-Emmett-Teller (BET) theory. The calculated BET specific surface areas revealed a pronounced and consistent upward trend directly correlated with the duration of acid corrosion treatment. The pristine TiO_2, serving as the baseline, exhibited a specific surface area of 39.9 m^2 g^{-1}. This value is characteristic of the initial, untreated material

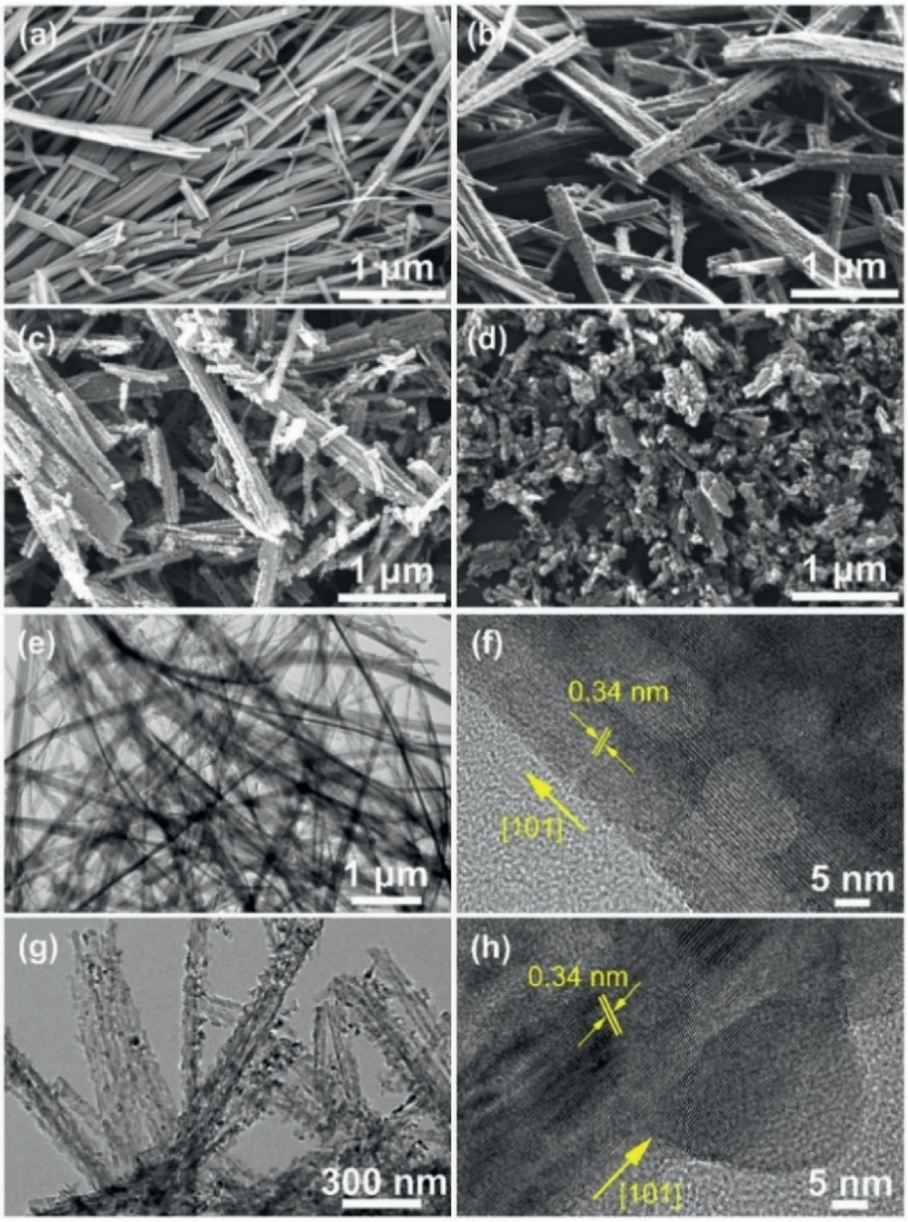

Fig. 1. Morphology characterization. (a–d) Typical SEM images of (a) pristine TiO_2 nanobelts and samples after acid corrosion for (b) 6 h, (c) 12 h, and (d) 24 h. (e–h) TEM and HRTEM images of (e,f) pristine TiO_2 and (g, h) TiO_2-12 h.

morphology. Upon subjecting the TiO_2 to acid corrosion for 6 h (TiO_2-6 h), the specific surface area increased measurably to 44.8 m^2 g^{-1}, indicating that the acid exposure had begun to modify the surface texture. Extending the corrosion duration to 12 h (TiO_2-12 h) resulted in a significantly higher specific surface area of 62.1 m^2 g^{-1}, representing a substantial increase of approximately 56 % compared to the pristine material. The maximum surface area was attained after the longest corrosion period of 24 h (TiO_2-24 h), reaching 68.1 m^2 g^{-1}. This final value corresponds to an impressive 71 % enhancement relative to the untreated TiO_2. The complete dataset is systematically presented in Table 1.

This progressive increase in specific surface area with extended acid exposure time is not merely a numerical observation; it provides strong quantitative evidence for significant microstructural and morphological alterations induced by the corrosive process. Acid corrosion typically acts by creating surface roughness and longer exposure times allow these etching mechanisms to proceed further. Consequently, the rising BET values directly reflect the creation of a more complex and extended surface architecture. The observed trend aligns perfectly with the distinct morphological evolution visualized through techniques such as SEM (Fig. 1a–d) and TEM (Fig. 1e–h) images. These images show increasing surface pitting, roughening, and particle fragmentation as corrosion time lengthens. The agreement between the quantified surface area increase (BET) and the qualitative/quantitative morphological analysis underscores the effectiveness of acid corrosion as a method for tailoring the textural properties of TiO_2. This enhanced surface area is expected to significantly impact the material's functional performance by providing more sites for interfacial reactions in its intended applications. The data unequivocally demonstrates that acid corrosion duration is a critical and controllable parameter for modulating the specific surface area of TiO_2.

The photocatalytic nitrogen reduction reaction performance of the synthesized TiO_2 samples (pristine and acid-corroded variants) was rigorously evaluated in ultrapure water without sacrificial agents using a custom-designed photoreactor [36,37], wherein a 300-W xenon lamp with AM 1.5G filter provided simulated solar irradiation. Prior to

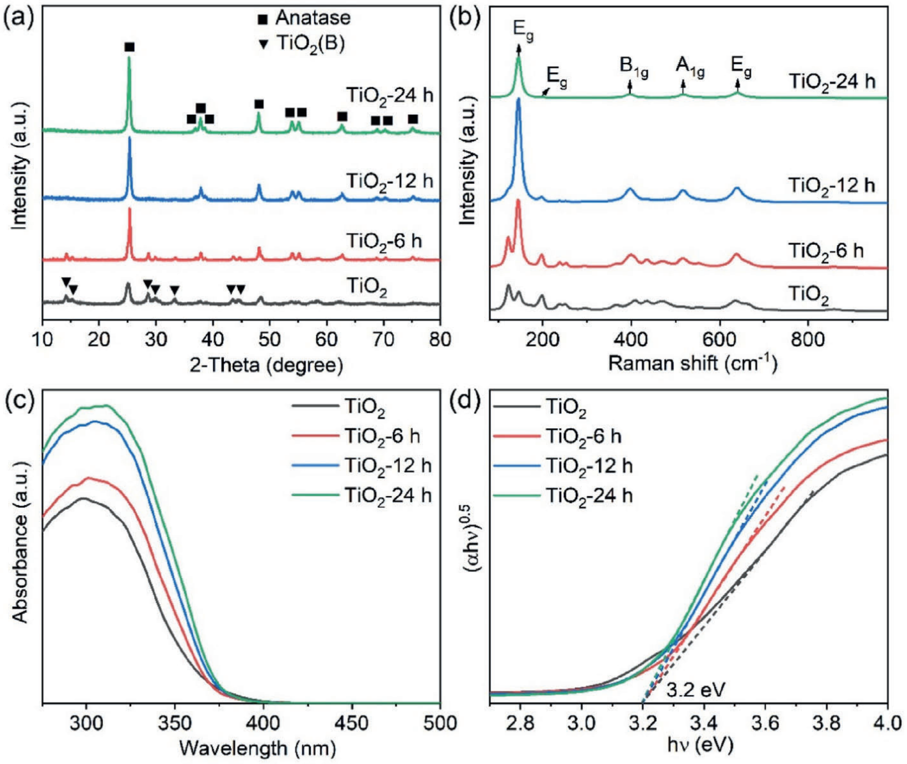

Fig. 2. Crystalline phase and optical characterizations: (a) XRD patterns, (b) Raman spectra, (c) UV–vis diffuse reflectance spectra (DRS), and (d) corresponding Tauc plots derived from (c).

Table 1
BET specific surface area of the catalysts.

Samples	BET surface area (m^2 g^{-1})	Morphology
TiO_2	39.9	Nanobelts
TiO_2-6 h	44.8	Nanobelts with less particles
TiO_2-12 h	62.1	Nanobelts with more particles
TiO_2-24 h	68.1	Fractured nanobelts

illumination, the suspension was purged with high-purity N_2 to ensure oxygen-free conditions and N_2 saturation. Photocatalytically generated ammonia was quantified via the indophenol blue method [15,36]. Fig. S1 demonstrates the absorbance spectra and visible color gradation for standard NH_4Cl solutions, confirming the linear correlation between chromophore intensity and NH^{4+} concentration. The absorbance peak at 679 nm was utilized to establish a calibration curve as shown in Fig. 3a, enabling precise determination of ammonia concentrations in experimental samples (Fig. 3b).

The results revealed a non-monotonic dependence of activity on acid corrosion duration that pristine TiO_2 exhibited a baseline production rate of 123.9 μg g_{cat}^{-1} h^{-1}, while TiO_2-6 h showed reduced activity (96.8 μg g_{cat}^{-1} h^{-1}), suggesting initial surface disruption. Strikingly, TiO_2-12 h achieved optimal performance at 219.9 μg g_{cat}^{-1} h^{-1}, which enhanced 77 % versus pristine TiO_2, and significantly surpassing TiO_2-24 h (77.0 μg g_{cat}^{-1} h^{-1}). This demonstrates that controlled acid corrosion effectively enhances photocatalytic nitrogen reduction reaction performance, with TiO_2-12 h delivering peak activity likely due to optimized surface properties balancing increased active sites and structural integrity. Critically, control experiments (Fig. 3c) verified the photocatalytic origin of ammonia. The results showed negligible ammonia under dark conditions (catalyst and N_2) and minimal yield without catalyst (light and water), but almost 5 times NH_3 yield enhancement under illumination conditions (catalyst, N_2 and light), which confirmed photocatalytic origin of ammonia. The ammonia in ultrapure water is close to the values reported in literatures [38,39]. The stability of a catalyst is a crucial performance indicator for evaluating its reusability. As shown in Fig. 3d, the TiO_2-12 h sample maintained its photocatalytic nitrogen fixation activity through five consecutive cycling tests with only a slight decrease in performance, demonstrating its relatively stable photocatalytic characteristics.

Following three consecutive photocatalytic reaction cycles, the harvested TiO_2-12 h photocatalyst was isolated from the suspension via centrifugation, washed thoroughly, and subjected to comprehensive structural characterization. XRD analysis reveals no detectable phase transformations or lattice alterations in the recycled material (Fig. 4a). High-resolution transmission electron microscopy (HRTEM) imaging unambiguously confirms the preserved belt-like nano-structural morphology without visible degradation or aggregation (Fig. S4). Furthermore, Raman spectroscopic examination (Fig. 4b) demonstrates completely maintained characteristic vibration modes, indicating undisturbed chemical bonding configurations after cycling. This multi-technique analytical evidence collectively attests to the exceptional structural integrity and operational stability of the TiO_2-12 h photocatalyst under prolonged reactive conditions.

To unambiguously confirm the nitrogenous origin of the generated ammonia, we performed comprehensive isotope labeling experiments using both $^{15}N_2$ and $^{14}N_2$ as feed gases. These isotopic tracers allow for definitive identification of nitrogen sources through their distinct nuclear magnetic resonance signatures. As shown in Fig. 5a, we first established a reference system by acquiring ^1H NMR spectra of $^{15}NH_4Cl$ standard solutions (dissolved in maleic acid buffer) across a concentration gradient from 30 to 120 μmol L^{-1}. The characteristic doublet peaks of $^{15}NH^{4+}$ at $\delta = 6.86$ and 7.05 ppm were clearly resolved, with their chemical shifts and coupling patterns serving as diagnostic fingerprints. The quantitative calibration curve in Fig. 5b was constructed by correlating the integrated peak area at 7.05 ppm with known $^{15}NH^{4+}$ concentrations, exhibiting excellent linearity across the tested range. Following photocatalytic reactions, ^1H NMR analysis of the reaction

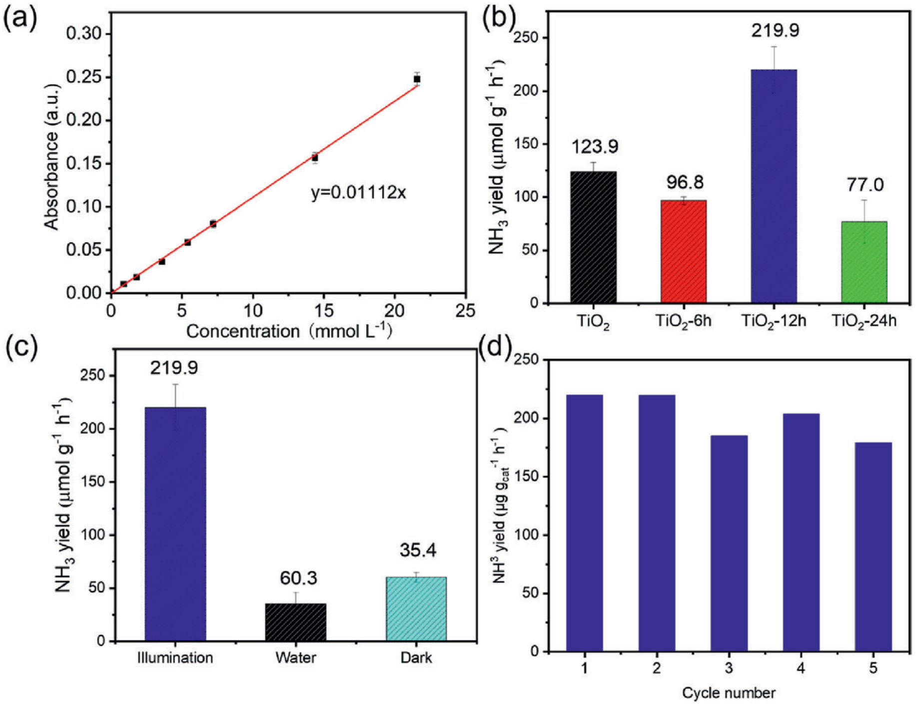

Fig. 3. Photocatalytic nitrogen fixation performance. (a) Ammonia calibration curve. (b) Ammonia production yield. (c) Control experiments confirming the photocatalytic origin of ammonia enhancement. Illumination means ultrapure water and catalyst under light (1 h, continuous N_2 bubbling). Dark means identical to "Illumination" without light. Water means ultrapure water without catalyst (N_2 bubbled for 1 h). (d) Cyclic photocatalytic tests demonstrating TiO_2-12 h stability.

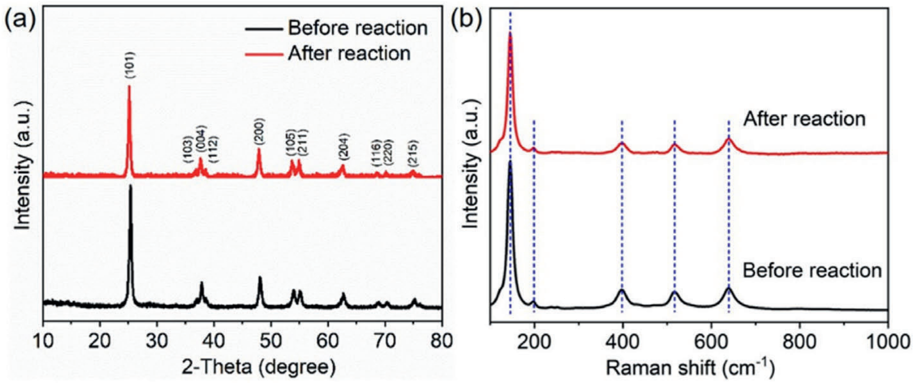

Fig. 4. Structural analysis of retrieved TiO_2-12 h photocatalyst after cyclic stability tests (see Fig. 3d). (a) XRD patterns. (b) Raman spectra.

solutions revealed striking isotopic differences. Systems fed with $^{15}N_2$ displayed the characteristic $^{15}NH_4^+$ doublet pattern, while $^{14}N_2$-fed controls exhibited the expected $^{14}NH_4^+$ triplet centered at 7.10 ppm (Fig. 5c) [40]. The absence of signal cross-contamination and the match with standard references provide irrefutable evidence that the detected ammonia originates exclusively from molecular nitrogen fixation, rather than potential nitrogen contaminants in the reaction system.

To identify the surface defects, XPS analysis was conducted. The O 1s spectrum (Fig. S5b) can be deconvoluted into multiple components. The peak at 532.68 eV corresponds to surface hydroxyl groups (-OH) generated by acid corrosion, while the peak at 531.64 eV is attributed to oxygen vacancies (OVs) in the TiO_2-24 h sample. This confirms that acid corrosion successfully introduces abundant OVs and modifies the surface chemistry. Correspondingly, the Ti 2p spectrum (Fig. S5c) shows characteristic peaks of Ti^{4+} at 465.88 eV and 459.28 eV. These results confirm that OVs are the crucial defect sites responsible for improving charge separation and N_2 adsorption [41]. To systematically investigate the abundance and distribution of surface defects in the photocatalyst, we employed electron spin resonance (ESR) spectroscopy to characterize transient free radical intermediates, particularly reactive oxygen species (ROS) generated during photocatalytic processes. As illustrated in Fig. 6a and b, the ESR spectra clearly demonstrate the formation of two critical radical species: hydroxyl radicals (·OH) and superoxide radicals ($\cdot O_2^-$). The highly polar nature of Ti-O bonds in TiO_2 induces strong surface polarization effects, which promote the dissociation of adsorbed water molecules and subsequent generation of these radical species through proton-coupled electron transfer processes. Control experiments conducted in the absence of light showed no detectable signals for either $\cdot O_2^-$ or ·OH, confirming the photoinduced nature of radical generation. Under visible light irradiation, characteristic four-line ESR spectra with 1:2:2:1 quartet for DMPO-·OH and 1:1:1:1 quartet for DMPO-$\cdot O_2^-$, respectively, were observed [42]. These results provide direct evidence for the photogeneration of both radical species during illumination. The presence of surface defects creates localized electron-rich regions that facilitate substantial negative charge accumulation on the TiO_2 surface. This phenomenon significantly enhances

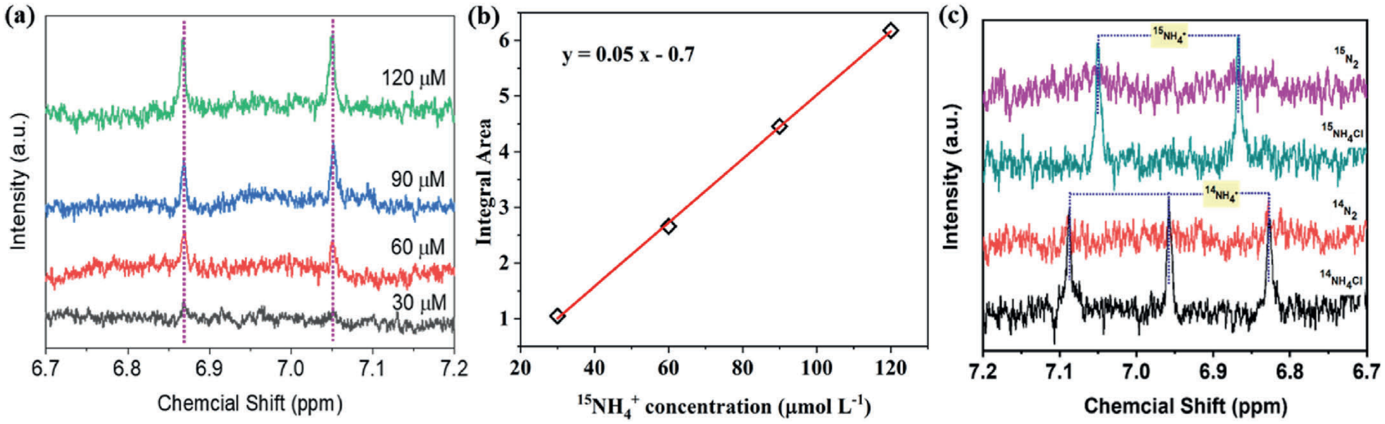

Fig. 5. (a) ^1H nuclear magnetic resonance (NMR) spectra of the standard $^{15}NH_4Cl$ solutions with concentrations of 30, 60, 90 and 120 μmol L^{-1}, (b) the corresponding calibration curve for determining the $^{15}NH_4^+$ concentration, (c) ^1H NMR spectra of the aqueous solutions fed with $^{15}N_2$ (upper) and $^{14}N_2$ (lower) after the photocatalytic reactions.

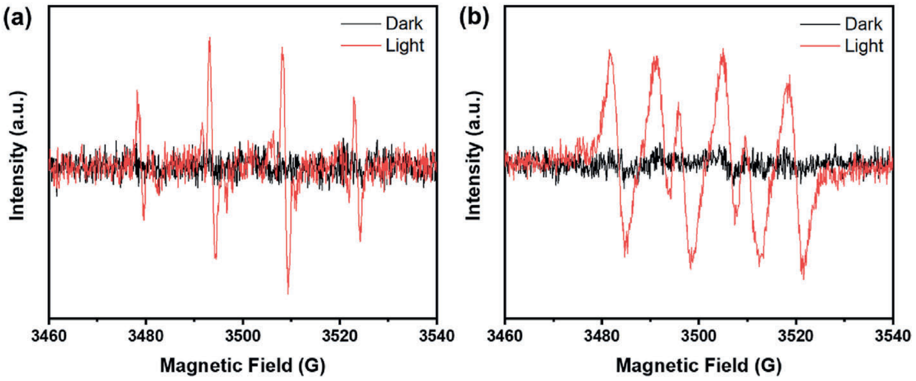

Fig. 6. ESR spectra of (a) hydroxyl radicals (•OH) and (b) superoxide radicals ($\bullet O_2^-$) generated by the sample.

efficient separation of photogenerated electron-hole pairs (shown also in Fig. 7a) and improved interfacial charge transfer kinetics. Collectively, these effects synergistically promote the multi-electron reduction of nitrogen to ammonia while suppressing charge recombination losses.

Our photocatalytic experiments demonstrate that TiO_2 nanobelts exhibit activity for nitrogen reduction reactions (NRR), with acid-etched TiO_2-12 h showing enhanced performance under UV light irradiation. To elucidate the underlying mechanism, we conducted systematic photoelectrochemical measurements to evaluate charge separation and transfer efficiencies. The photocurrent responses of the samples under 50 s intermittent visible light irradiation are presented in Fig. 7a. The pristine TiO_2 electrode exhibits a photocurrent density of 0.05 μA cm^{-2}. After acid corrosion, the photocurrent densities of the corroded TiO_2 electrodes are significantly enhanced, with TiO_2-12 h reaching the highest value of 0.25 μA cm^{-2}, which is consistent with the photocatalytic experiment [3,43]. The reproducible photocurrent responses over multiple cycles suggest excellent stability of the catalysts, which benefits from the efficient charge separation and the effective transfer of photoinduced electrons to the external circuit. The conclusion is further corroborated by photoluminescence (PL) spectroscopy (Fig. 7b). The pristine TiO_2 nanobelts display a broad emission peak centered at ~520 nm, characteristic of defect-related recombination. In contrast, TiO_2-12

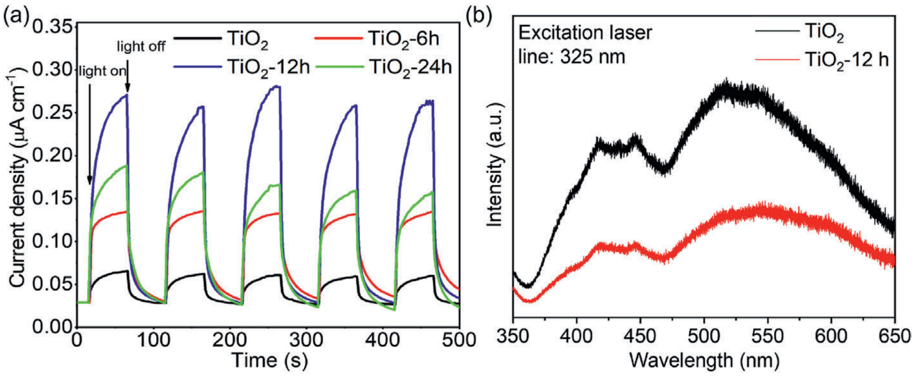

Fig. 7. (a) Photocurrent responses of TiO_2 with different acid corrosion times under intermittent visible light (b) Comparative photoluminescence (PL) emission spectra of pristine TiO_2 and acid-etched TiO_2-12 h samples recorded at an excitation wavelength of 325 nm.

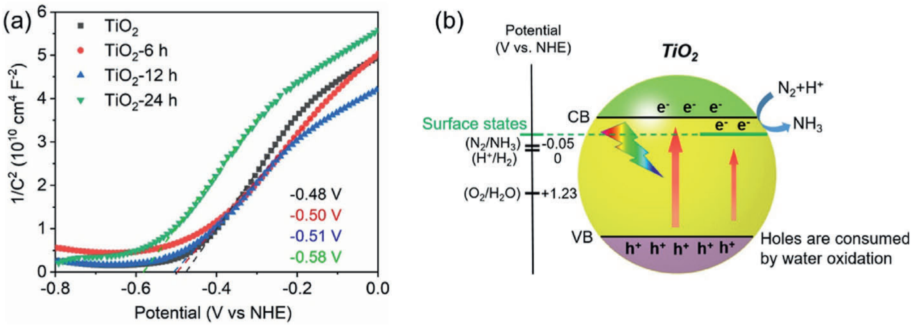

Fig. 8. (a) Mott-Schottky plots of pristine TiO_2 and acid-etched samples of TiO_2-6 h, TiO_2-12 h, TiO_2-24 h. (b) Schematic illustration of photocatalytic mechanism.

h shows markedly quenched PL intensity, confirming the effective inhibition of radiative recombination pathways. These findings are consistent with recent studies on engineered TiO_2-based photocatalysts [44], where reduced PL intensity directly correlates with improved charge separation. The synergistic combination of photoelectrochemical and spectroscopic analyses provides compelling evidence that acid etching creates additional active sites for NRR and enhances charge separation efficiency as well as prolongs carrier lifetimes, all contributing to the observed photocatalytic improvement.

As discussed previously, photocatalytic performance is critically dependent on charge carrier dynamics. A major factor limiting performance is the recombination of photogenerated electron-hole pairs, which can occur either in the bulk phase or at the catalyst surface. To investigate the fundamental parameters governing charge transport, we performed Mott-Schottky measurements to determine the flat-band potentials of the catalysts (Fig. 8a). Mott-Schottky analysis provides two key parameters of the flat-band potential and the donor density. The former one is obtained from the intercept of the extrapolated linear region with the potential axis [45,46]. This potential represents the equilibrium condition where the semiconductor's Fermi level aligns with the electrolyte's redox potential [47]. While the donor density (for n-type TiO_2) can be derived from the slope of the linear region. Our measurements reveal that the flat-band potential values for pristine TiO_2 nanobelts, TiO_2-6 h, TiO_2-12 h, and TiO_2-24 h are −0.48, −0.50, −0.51, and −0.58 V (vs. NHE), respectively. For n-type semiconductors, the conduction band minimum (CBM) typically lies ~0.1 eV above flat-band potential, yielding CBM positions of −0.58, −0.60, −0.61, and −0.68 V. Combined with the consistent bandgap of 3.2 eV (from Tauc plots in Fig. 2d), the valence band maxima (VBM) are calculated as 2.62, 2.60, 2.59, and 2.52 V, respectively. Notably, acid etching induces a systematic negative shift in flat-band potential that correlates with treatment duration. Given the constant electrolyte conditions (pH and redox species), this shift likely arises from increased surface states near the Fermi level. TEM analysis (Fig. 1h and Fig. S3) confirms these states originate from grain boundaries between secondary structures and defects on newly formed nanoparticles.

The negative shift in flat-band potentials promotes the transfer of photogenerated electrons from the conduction band of TiO_2 to surface-adsorbed redox species [48,49]. As shown in Fig. 8b, upon UV irradiation, electrons in TiO_2 nanobelts are excited from the valence band to the conduction band, leaving holes in the valence band. The photoexcited electrons then migrate to the catalyst surface, where they reduce adsorbed N_2 molecules, while the holes in the valence band are consumed by the water oxidation reaction. Although surface defects can lower the energy barrier for the nitrogen reduction reaction, they may also act as trap centers that enhance the recombination of photogenerated charges [50,51]. Nevertheless, these defects accelerated transfer of photogenerated electrons from TiO_2 to the empty anti-bonding orbitals (π^*) of adsorbed N_2, thereby promoting N_2 activation and cleavage of the $N \equiv N$ triple bond [52].

This dual role was further quantified through donor density calculations derived from Mott-Schottky analysis [53,54], where the slope of the linear region provides the carrier concentration according to:

$$N_b = \left(\frac{2}{e\varepsilon\varepsilon_0}\right)\left[\frac{d\left(1/C^2\right)}{dV}\right]^{-1}$$

where N_d is the donor density, e is the electron charge, ε is the dielectric constant, and ε_0 is the vacuum permittivity. The donor densities of pristine TiO_2, TiO_2-6 h, TiO_2-12 h, and TiO_2-24 h were measured as 1.95 × 10^{19}, 2.42 × 10^{19}, 2.55 × 10^{19}, and 2.08 × 10^{19} cm^{-3}, respectively, demonstrating that acid etching treatment generally increased carrier concentration. While extended etching duration (up to 12 h) enhanced this effect when the nanobelt morphology was preserved, the particulate TiO_2-24 h showed reduced donor density likely due to excessive surface defects promoting charge recombination [55,56]. The well-crystallized 1D structure of pristine TiO_2 nanobelts facilitates rapid electron transport but suffers from limited interfacial charge transfer due to insufficient surface active sites [57], resulting in modest photocatalytic activity. Complete morphological transformation into nanoparticles increases surface active sites but introduces grain boundaries that impede electron transport, while additional surface defects act as recombination centers for electron-hole pairs [58], explaining the lowest photocurrent density observed for TiO_2-24 h. These results demonstrate that effective photocatalytic nitrogen reduction requires surface defects as active sites for charge transfer, but defect density must be carefully optimized to balance activity and recombination. Although the current performance of optimized TiO_2 nanobelts falls short of practical requirements, their structural properties make them promising substrates for developing composite photocatalysts for nitrogen fixation applications.

4. Conclusions

In summary, one-dimensional TiO_2 nanobelts were synthesized via a facile hydrothermal method, followed by controlled acid etching to modulate their surface architecture. Comprehensive SEM and TEM characterization revealed that the acid treatment generated secondary nanostructures on the TiO_2 nanobelt surfaces, which simultaneously increased active sites for nitrogen reduction and modified charge carrier dynamics. The optimized TiO_2-12 h photocatalyst demonstrated superior performance, achieving an ammonia production rate of 219.9 μg g_{cat}^{-1} h^{-1} under standard conditions. Systematic photoelectrochemical analysis, including transient photocurrent measurements and photoluminescence spectroscopy, confirmed that moderate acid etching optimally regulates charge separation and transfer processes. This study establishes TiO_2 nanobelts as promising foundational materials for developing advanced composite photocatalysts toward sustainable ammonia synthesis through photocatalytic nitrogen fixation.

CRediT authorship contribution statement

Guanzheng Liu: Investigation, Formal analysis, Data curation.

Mengyu Wang: Data curation. **Jianing Huang:** Investigation, Formal analysis, Data curation. **Chunyuan Li:** Investigation, Formal analysis, Data curation. **Junkai Ren:** Methodology, Formal analysis, Conceptualization. **Qi Wang:** Writing – review & editing. **Haili Pang:** Formal analysis. **Hui Zhang:** Writing – review & editing. **Xiaoxia Bai:** Writing – review & editing, Supervision, Resources, Methodology, Funding acquisition, Conceptualization.

Declaration of competing interest

The authors declare the following financial interests/personal relationships which may be considered as potential competing interests: Junkai Ren reports was provided by Xidian University. If there are other authors, they declare that they have no known competing financial interests or personal relationships that could have appeared to influence the work reported in this paper.

Acknowledgments

This work was supported by the National Natural Science Foundation of China (6217032156, 52202294), the National Key Research and Development Program of China (2019YFE0121600), Xidian University Specially Funded Project for Interdisciplinary Exploration (TZJH2024046), Shaanxi Province high foreign expertise project (90728220020), Research start-up funds (10251220007), and the Fundamental Research Funds for the Central Universities (JB211412). The shared facilities of Analysis and Test Center of Xidian University.

Appendix A. Supplementary data

Supplementary data to this article can be found online at https://doi.org/10.1016/j.pnsc.2025.11.004.

References

[1] B.M. Hoffman, D.R. Dean, L.C. Seefeldt, Climbing nitrogenase: toward a mechanism of enzymatic nitrogen fixation, Accounts Chem. Res. 42 (2009) 609–619, https://doi.org/10.1021/ar8002128.

[2] J.G. Chen, R.M. Crooks, L.C. Seefeldt, K.L. Bren, R.M. Bullock, M.Y. Darensbourg, P.L. Holland, B. Hoffman, M.J. Janik, A.K. Jones, M.G. Kanatzidis, P. King, K. M. Lancaster, S.V. Lymar, P. Pfromm, W.F. Schneider, R.R. Schrock, Beyond fossil fuel–driven nitrogen transformations, Science 360 (2018) eaar6611, https://doi.org/10.1126/science.aar6611.

[3] Z. Zhao, S. Hong, C. Yan, C. Choi, Y. Jung, Y. Liu, S. Liu, X. Li, J. Qiu, Z. Sun, Efficient visible-light driven n2 fixation over two-dimensional Sb/TiO_2 composites, Chem. Commun. 55 (2019), https://doi.org/10.1039/C9CC02291K.

[4] R. Shi, X. Zhang, G.I.N. Waterhouse, Y. Zhao, T. Zhang, The journey toward low temperature, low pressure catalytic nitrogen fixation, Adv. Energy Mater. 10 (2020) 2000659, https://doi.org/10.1002/aenm.202000659.

[5] J. Ran, A. Talebian-Kiakalaieh, S.-Z. Qiao, Atomically-scattered active centers accelerating photocatalytic evolution of ammonia, Adv. Energy Mater. 14 (2024) 2400650, https://doi.org/10.1002/aenm.202400650.

[6] L. Shi, Y. Yin, S.B. Wang, H.Q. Sun, Rational catalyst design for N reduction under ambient conditions: strategies toward enhanced conversion efficiency, ACS Catal. 10 (2020) 6870–6899, https://doi.org/10.1021/acscatal.0c01081.

[7] N. Ben Saber, A. Mezni, A. Alrooqi, T. Altalhi, Fabrication of efficient Au@TiO_2/rgo heterojunction nanocomposite: boosted photocatalytic activity under ultraviolet and visible light irradiation, J. Mater. Res. Technol. 12 (2021) 2238–2246, https://doi.org/10.1016/j.jmrt.2021.03.109.

[8] S.K. Cushing, J.T. Li, F.K. Meng, T.R. Senty, S. Suri, M.J. Zhi, M. Li, A.D. Bristow, N. Q. Wu, Photocatalytic activity enhanced by plasmonic resonant energy transfer from metal to semiconductor, J. Am. Chem. Soc. 134 (2012) 15033–15041, https://doi.org/10.1021/ja305603t.

[9] A.J. Medford, M.C. Hatzell, Photon-driven nitrogen fixation: current progress, thermodynamic considerations, and future outlook, ACS Catal. 7 (2017) 2624–2643, https://doi.org/10.1021/acscatal.7b00439.

[10] W.M. Ding, Y. Yang, X.M. Li, S.B. Yuan, R.Y. Shi, Z.Y. Liu, M. Luo, Single-atom mo supported by TiO_2 for photocatalytic nitrogen fixation, Langmuir 41 (2024) 340–349, https://doi.org/10.1021/acs.langmuir.4c03624.

[11] Y. Huang, N. Zhang, Z. Wu, X. Xie, Artificial nitrogen fixation over bismuth-based photocatalysts: fundamentals and future perspectives, J. Mater. Chem. A 8 (2020) 4978–4995, https://doi.org/10.1039/C9TA13589H.

[12] S. Wang, F. Ichihara, H. Pang, H. Chen, J. Ye, Nitrogen fixation reaction derived from nanostructured catalytic materials, Adv. Funct. Mater. 28 (2018) 1803309, https://doi.org/10.1002/adfm.201803309.

[13] Z.H. Wang, X. Hu, Z.Z. Liu, G.J. Zou, G.N. Wang, K. Zhang, Recent developments in polymeric carbon nitride-derived photocatalysts and electrocatalysts for nitrogen fixation, ACS Catal. 9 (2019) 10260–10278, https://doi.org/10.1021/acscatal.9b03015.

[14] M.A. Arvizu, F.J. González, A. Romero-Galarza, F.J. Rodríguez-Varela, C.R. Garcia, M.A. Garcia-Lobato, Symmetric supercapacitors of pani coated RuO_2/TiO_2 macroporous structures prepared by electrostatic spray deposition, J. Electrochem. Soc. 169 (2022) 020564, https://doi.org/10.1149/1945-7111/ac5482.

[15] Y.X. Bai, Y.Z. Wang, J.Y. Chen, K.D. Zhu, J.J. Wang, Efficient and highly selective photocatalytic reduction of cr(vi) by an active two-dimensional covalent organic framework, Prog. Nat Sci-Mater. 34 (2024) 933–941, https://doi.org/10.1016/j.pnsc.2024.09.004.

[16] Y. Chen, Q. Sun, Z. Ni, X. Tu, C. Sun, S. Zhu, X. Duan, M. Jiang, Z. Xie, M. Liu, H. Zheng, High-efficient solar-driven nitrogen fixation by modulating the internal electric-field of mofs via n-site-enhanced charge density difference in organic ligands, Chem. Eng. J. 482 (2024) 148853, https://doi.org/10.1016/j.cej.2024.148853.

[17] A.A. Ashkarran, M. Fakhari, H. Hamidinezhad, H. Haddadi, M.R. Nourani, TiO_2 nanoparticles immobilized on carbon nanotubes for enhanced visible-light photo-induced activity, J. Mater. Res. Technol. 4 (2015) 126–132, https://doi.org/10.1016/j.jmrt.2014.10.005.

[18] H. Hirakawa, M. Hashimoto, Y. Shiraishi, T. Hirai, Photocatalytic conversion of nitrogen to ammonia with water on surface oxygen vacancies of titanium dioxide, J. Am. Chem. Soc. 139 (2017) 10929–10936, https://doi.org/10.1021/jacs.7b06634.

[19] D. Zhu, L. Zhang, R.E. Ruther, R.J. Hamers, Photo-illuminated diamond as a solid-state source of solvated electrons in water for nitrogen reduction, Nat. Mater. 12 (2013) 836–841, https://doi.org/10.1038/nmat3696.

[20] L. Li, Y. Wang, S. Vanka, X. Mu, Z. Mi, C.-J. Li, Nitrogen photofixation over III-nitride nanowires assisted by ruthenium clusters of low atomicity, Angew. Chem. Int. Ed. 56 (2017) 8701–8705, https://doi.org/10.1002/anie.201703301.

[21] X. Ge, X. Zheng, T. Zhou, L.-J. Tian, W. Wang, J.-j. Chen, X. Wang, Engineering spin state of atomic iron centers for high-performance photocatalytic nitrogen fixation, Angew. Chem. Int. Ed. 64 (2025) e202506470, https://doi.org/10.1002/anie.202506470.

[22] X. Wang, Y. Li, L. Feng, Y. Yang, X. Zheng, Construction of BiOBr/hydrophobic carbon cloth heterojunction with internal electric field for enhanced photocatalytic nitrogen fixation, Small 21 (2025) e03853, https://doi.org/10.1002/smll.202503853.

[23] Z. Zhong, H.-J. Zhang, Y.-Y. Yang, T.-K. Zhang, X.-H. Qu, L. Ma, H.-L. Cao, Y.-D. Hou, J. Lü, Oxygen and bromine vacancies synergistically induce local polarization electric field for enhanced photocatalytic nitrogen fixation on BiOBr, ACS Catal. 15 (2025) 6334–6345, https://doi.org/10.1021/acscatal.5c00818.

[24] A. Alshehri, K. Narasimharao, PtO_x-TiO_2 anatase nanomaterials for photocatalytic reformation of methanol to hydrogen: effect of TiO_2 morphology, J. Mater. Res. Technol. 9 (2020) 14907–14921, https://doi.org/10.1016/j.jmrt.2020.10.087.

[25] A. Ganesan, S. Alhowity, A.Z. Alsaleh, M. Guragain, O. Omolere, T.R. Cundari, J. Kelber, F. D'Souza, Electro- and photocatalytic conversion of N_2 to NH_3 by chemically modified transition metal dichalcogenides, MoS_2, and WS_2, J. Electrochem. Soc. 170 (2023) 056501, https://doi.org/10.1149/1945-7111/acd02d.

[26] A. García-Eguizábal, M. Gomez Mendoza, M. Barawi, L. Collado, A. Sánchez-Ruiz, J.C. García Martínez, M. Liras, V.A. de la Peña O'Shea, Nanostructuration effect of carbon-based phenylene vinylene conjugated porous polymers on TiO_2 hybrid materials for artificial photosynthesis, Small Struct. 5 (2024) 2300410, https://doi.org/10.1002/sstr.202300410.

[27] Z. Zhao, J. Tian, Y. Sang, A. Cabot, H. Liu, Structure, synthesis, and applications of TiO_2 nanobelts, Adv. Mater. 27 (2015) 2557–2582, https://doi.org/10.1002/adma.201405589.

[28] G.N. Schrauzer, T.D. Guth, Photolysis of water and photoreduction of nitrogen on titanium dioxide, J. Am. Chem. Soc. 99 (1977) 7189–7193, https://doi.org/10.1021/ja00464a015.

[29] K.M.S.D.B. Kulathunga, C.-F. Yan, J. Bandara, Photocatalytic removal of airborne indoor pollutants by ir illuminated silver coated TiO_2 catalyst: advantage of one-dimensional TiO_2 nanostructures in ir active photocatalysis, Colloids Surf. A Physicochem. Eng. Asp. 590 (2020) 124509, https://doi.org/10.1016/j.colsurfa.2020.124509.

[30] Y. Zhang, X. Chen, S. Zhang, L. Yin, Y. Yang, Defective titanium dioxide nanobamboo arrays architecture for photocatalytic nitrogen fixation up to 780 nm, Chem. Eng. J. 401 (2020) 126033, https://doi.org/10.1016/j.cej.2020.126033.

[31] R. Liu, C. Lu, X. Ding, Y. Cai, S. Liang, Polyimide/titanium dioxide self-cleaning nano-hybrid films with high photocatalytic properties, Prog. Nat. Sci. Mater. Int. 33 (2023) 674–680, https://doi.org/10.1016/j.pnsc.2023.12.003.

[32] Z. Zhao, J. Tian, D. Wang, X. Kang, Y. Sang, H. Liu, J. Wang, S. Chen, R. I. Boughton, H. Jiang, Uv-visible-light-activated photocatalysts based on Bi_2O_3/$Bi_4Ti_3O_{12}$/TiO_2 double-heterostructured TiO_2 nanobelts, J. Mater. Chem. 22 (2012) 23395–23403, https://doi.org/10.1039/C2JM34580C.

[33] X. Pan, Y. Zhao, S. Liu, C.L. Korzeniewski, S. Wang, Z. Fan, Comparing graphene-TiO_2 nanowire and graphene-TiO_2 nanoparticle composite photocatalysts, ACS Appl. Mater. Interfaces 4 (2012) 3944–3950, https://doi.org/10.1021/am300772t.

[34] M.-V. Sofianou, M. Tassi, V. Psycharis, N. Boukos, S. Thanos, T. Vaimakis, J. Yu, C. Trapalis, Solvothermal synthesis and photocatalytic performance of Mn^{4+}-doped anatase nanoplates with exposed {001} facets, Appl. Catal. B Environ. 162 (2015) 27–33, https://doi.org/10.1016/j.apcatb.2014.05.049.

[35] P. Wu, T. Zhou, Z. Tong, F. Xi, J. Lu, X. Li, W. Ma, S. Li, X. Yang, Balancing charge carrier density and exciton recombination in defective g-C_3N_4 for efficient

photocatalytic hydrogen evolution, Prog. Nat. Sci. Mater. Int. 35 (2025) 238–244, https://doi.org/10.1016/j.pnsc.2024.12.015.

[36] Y. Li, S. Zhang, P. Yang, Y. Yang, F. Chen, X. Liu, M. Li, Enhanced electrochemical oxidation of benzene and toluene in aqueous environments using Sb–SnO_2-doped TiO_2 nanotubes modified by hydrophobic polytetrafluoroethylene (PTFE), Prog. Nat. Sci. Mater. Int. 34 (2024) 1009–1020, https://doi.org/10.1016/j.pnsc.2024.07.017.

[37] J. Luo, X. Bai, Q. Li, X. Yu, C. Li, Z. Wang, W. Wu, Y. Liang, Z. Zhao, H. Liu, Band structure engineering of bioinspired Fe doped $SrMoO_4$ for enhanced photocatalytic nitrogen reduction performance, Nano Energy 66 (2019) 104187, https://doi.org/10.1016/j.nanoen.2019.104187.

[38] J. Ding, Q. Zhong, H. Gu, Iron-titanium dioxide composite nanoparticles prepared with an energy effective method for efficient visible-light-driven photocatalytic nitrogen reduction to ammonia, J. Alloys Compd. 746 (2018) 147–152, https://doi.org/10.1016/j.jallcom.2018.01.362.

[39] J. Yang, Y. Guo, R. Jiang, F. Qin, H. Zhang, W. Lu, J. Wang, J.C. Yu, High-efficiency "working-in-tandem" nitrogen photofixation achieved by assembling plasmonic gold nanocrystals on ultrathin titania nanosheets, J. Am. Chem. Soc. 140 (2018) 8497–8508, https://doi.org/10.1021/jacs.8b03537.

[40] Y. Wang, W. Zhou, R. Jia, Y. Yu, B. Zhang, Unveiling the activity origin of a copper-based electrocatalyst for selective nitrate reduction to ammonia, Angew. Chem. Int. Ed. 59 (2020) 5350–5354, https://doi.org/10.1002/anie.201915992.

[41] W. Zhang, L. Cai, S. Cao, L. Qiao, Y. Zeng, Z. Zhu, Z. Lv, H. Xia, L. Zhong, H. Zhang, X. Ge, J. Wei, S. Xi, Y. Du, S. Li, X. Chen, Interfacial lattice-strain-driven generation of oxygen vacancies in an aerobic-annealed TiO_2(b) electrode, Adv. Mater. 31 (2019) 1906156, https://doi.org/10.1002/adma.201906156.

[42] X. Su, X. Zhang, L. Hu, M. Gao, S. Yao, Y. Lu, M. Zhao, W. Zhou, H. Zhang, Y. Ren, T. Wei, J. Feng, Lattice disorder driving the electron migration from tetracycline to TiO_2 via ligand-to-metal charge transfer to generate superoxide radical, Separ. Purif. Technol. 353 (2025) 128614, https://doi.org/10.1016/j.seppur.2024.128614.

[43] W. Zhao, J. Zhang, X. Zhu, M. Zhang, J. Tang, M. Tan, Y. Wang, Enhanced nitrogen photofixation on Fe-doped TiO_2 with highly exposed (101) facets in the presence of ethanol as scavenger, Appl. Catal. B Environ. 144 (2014) 468–477, https://doi.org/10.1016/j.apcatb.2013.07.047.

[44] Q. Liu, L. Ai, J. Jiang, MXene-derived TiO_2@C/g-C_3N_4 heterojunctions for highly efficient nitrogen photofixation, J. Mater. Chem. A 6 (2018) 4102–4110, https://doi.org/10.1039/C7TA09350K.

[45] J. Chen, B. Li, J. Zheng, S. Jia, J. Zhao, H. Jing, Z. Zhu, Role of one-dimensional ribbonlike nanostructures in dye-sensitized TiO_2-based solar cells, J. Phys. Chem. C 115 (2011) 7104–7113, https://doi.org/10.1021/jp2004369.

[46] K. Gelderman, L. Lee, S.W. Donne, Flat-band potential of a semiconductor: using the mott–schottky equation, J. Chem. Educ. 84 (2007) 685, https://doi.org/10.1021/ed084p685.

[47] Y. Chen, L. Lin, W. Xu, C. Liu, C. Yu, Y. Cheng, R. Qi, R. Huang, Origin of cycle performance in the Ag_2O/TiO_2 heterostructure photocatalyst, Langmuir 39 (2023) 14904–14911, https://doi.org/10.1021/acs.langmuir.3c01675.

[48] Z. Dastani, Y. Absalan, M. Gholizadeh, O. Kovalchukova, A composite of 2-aminoterephthalic acid coupled with TiF_3@TiO_2/polyvinyl alcohol with enhanced visible-light photocatalytic reactivity; investigation of the photocatalytic mechanism, J. Mater. Res. Technol. 15 (2021) 7158–7173, https://doi.org/10.1016/j.jmrt.2021.11.139.

[49] Y. Zhao, Y. Zhao, R. Shi, B. Wang, G.I.N. Waterhouse, L.-Z. Wu, C.-H. Tung, T. Zhang, Tuning oxygen vacancies in ultrathin TiO_2 nanosheets to boost photocatalytic nitrogen fixation up to 700 nm, Adv. Mater. 31 (2019) 1806482, https://doi.org/10.1002/adma.201806482.

[50] Q. Gui, Z. Xu, H. Zhang, C. Cheng, X. Zhu, M. Yin, Y. Song, L. Lu, X. Chen, D. Li, Enhanced photoelectrochemical water splitting performance of anodic TiO_2 nanotube arrays by surface passivation, ACS Appl. Mater. Interfaces 6 (2014) 17053–17058, https://doi.org/10.1021/am504662w.

[51] Y. Yan, H. Yang, X. Zhao, R. Li, X. Wang, Enhanced photocatalytic activity of surface disorder-engineered $CaTiO_3$, Mater. Res. Bull. 105 (2018) 286–290, https://doi.org/10.1016/j.materresbull.2018.05.008.

[52] S. Wang, X. Hai, X. Ding, K. Chang, Y. Xiang, X. Meng, Z. Yang, H. Chen, J. Ye, Light-switchable oxygen vacancies in ultrafine Bi_5O_7br nanotubes for boosting solar-driven nitrogen fixation in pure water, Adv. Mater. 29 (2017) 1701774, https://doi.org/10.1002/adma.201701774.

[53] D. Li, Y. Li, D. Liao, M. Cao, L. Zhang, S. Zhang, L. Chen, Y. Chen, H. Wang, J. Qi, F. You, Enhanced light harvesting ability in hollow Pt/TiO_2 nanoreactor for boosting tetracycline photodegradation, Prog. Nat. Sci. Mater. Int. 34 (2024) 767–775, https://doi.org/10.1016/j.pnsc.2024.07.005.

[54] Y. Zhang, H. Zhang, S. Tian, L. Zhang, W. Li, W. Wang, X. Yan, N. Han, X. Zhang, The photocatalysis-enhanced TiO_2@hpan membrane with high tio_2 surface content for highly effective removal of cationic dyes, Langmuir 37 (2021) 9415–9428, https://doi.org/10.1021/acs.langmuir.1c01066.

[55] H. Fang, Y. Kang, S. Yuan, M. Zhang, Z. Rui, One step synthesis and interfacial properties of black Ag/$Tio_{2\text{-}x}$ for enhancing sunlight absorption with application to photothermocatalytic vocs degradation, Appl. Surf. Sci. 655 (2024) 159519, https://doi.org/10.1016/j.apsusc.2024.159519.

[56] L. Liccardo, M. Bordin, P.M. Sheverdyaeva, M. Belli, P. Moras, A. Vomiero, E. Moretti, Surface defect engineering in colored Tio_2 hollow spheres toward efficient photocatalysis, Adv. Funct. Mater. 33 (2023) 2212486, https://doi.org/10.1002/adfm.202212486.

[57] M. Fazil, S.M. Alshehri, Y. Mao, T. Ahmad, Enhanced photo/electrocatalytic hydrogen evolution by hydrothermally derived Cu-doped Tio_2 solid solution nanostructures, Langmuir 40 (2024) 4063–4076, https://doi.org/10.1021/acs.langmuir.3c02860.

[58] H. Chen, Z. Fan, Z.-C. Zhang, J. Guo, C.-C. Wang, Synthesis and modification of g-C_3N_4 semiconductor catalysts for photocatalytic hydrogen evolution: a review, Prog. Nat. Sci. Mater. Int. 35 (2025) 449–468, https://doi.org/10.1016/j.pnsc.2025.03.007.